Frontiers of Information Technology & Electronic Engineering
www.jzus.zju.edu.cn; engineering.cae.cn; www.springerlink.com
ISSN 2095-9184 (print); ISSN 2095-9230 (online)
E-mail: jzus@zju.edu.cn

Ka-band broadband filtering packaging antenna based on through-glass vias (TGVs)*

Zhen FANG†[1,2], Jihua ZHANG†‡[1,2,3], Libin GAO[1,2], Hongwei CHEN[1,2], Wenlei LI[1,2], Tianpeng LIANG[1,2], Xudong CAI[1,2], Xingzhou CAI[3], Weicong JIA[3], Huan GUO[3], Yong LI[3]

[1]*School of Integrated Circuit Science and Engineering, University of Electronic Science and Technology of China, Chengdu 610054, China*

[2]*State Key Laboratory of Electronic Thin Films and Integrated Devices, University of Electronic Science and Technology of China, Chengdu 610054, China*

[3]*Chengdu Micro-Technology Co., Ltd., Chengdu 611731, China*

†E-mail: zhenfang@std.uestc.edu.cn; jhzhang@uestc.edu.cn

Received Nov. 17, 2022; Revision accepted Jan. 6, 2023; Crosschecked Mar. 17, 2023

Abstract: This work presents a novel design of Ka-band (33 GHz) filtering packaging antenna (FPA) that features broadband and great filtering response, and is based on glass packaging material and through-glass via (TGV) technologies. Compared to traditional packaging materials (printed circuit board, low temperature co-fired ceramic, Si, etc.), TGVs are more suitable for miniaturization (millimeter-wave three-dimensional (3D) packaging devices) and have superior microwave performance. Glass substrate can realize 3D high-density interconnection through bonding technology, while the coefficient of thermal expansion (CTE) matches that of silicon. Furthermore, the stacking of glass substrate enables high-density interconnections and is compatible with micro-electro-mechanical system technology. The proposed antenna radiation patch is composed of a patch antenna and a bandpass filter (BPF) whose reflection coefficients are almost complementary. The BPF unit has three pairs of $\lambda_g/4$ slots (defect microstrip structure, DMS) and two $\lambda_g/2$ U-shaped slots (defect ground structure, DGS). The proposed antenna achieves large bandwidth and high radiation efficiency, which may be related to the stacking of glass substrate and TGV feed. In addition, the introduction of four radiation nulls can effectively improve the suppression level in the stopband. To demonstrate the performance of the proposed design, a 33-GHz broadband filtering antenna is optimized, debugged, and measured. The antenna could achieve $|S_{11}|<-10$ dB in 29.4–36.4 GHz, and yield an impedance matching bandwidth up to 21.2%, with the stopband suppression level at higher than 16.5 dB. The measurement results of the proposed antenna are a realized gain of ~6.5 dBi and radiation efficiency of ~89%.

Key words: Filtering packaging antenna (FPA); Through-glass vias (TGVs); 3D packaging devices; Laser bonding
https://doi.org/10.1631/FITEE.2200573 **CLC number:** TN828.6

1 Introduction

With the booming growth of smart phone technology, high-performance computing, artificial intelligence, and other emerging fields, millimeter-wave antennas are becoming increasingly prevalent in communication systems (Zhang XY et al., 2015, 2017; Hu PF et al., 2016, 2019; Hwang et al., 2017; Li WX et al., 2017; El-Halwagy et al., 2018; Jin et al., 2018; Li JF et al., 2018, 2021; Shah et al., 2018; Wu et al., 2018; Zhang BH and Xue, 2018; Cao et al., 2020; He et al., 2020; Hu KZ et al., 2020; Liu et al., 2020; Watanabe et al., 2020; Xia et al., 2020; Yao et al., 2020; Chen et al., 2021; Shao and Zhang, 2021; Fang et al., 2022; Hu HT et al., 2022; Su et al., 2022; Li WL et al., 2023). Microstrip antennas are widely used in millimeter-wave antenna design due to their low profile, simple

‡ Corresponding author
* Project supported by the Fundamental Research Funds for the Central Universities, China (No. ZYGX2019Z003)
ORCID: Zhen FANG, https://orcid.org/0000-0001-8482-8013

manufacturing process, and easy integration (Li WX et al., 2017; He et al., 2020; Chen et al., 2021; Shao and Zhang, 2021; Fang et al., 2022; Hu HT et al., 2022; Su et al., 2022). Meanwhile, various new applications demand higher requirements for advanced packaging (Shah et al., 2018; Chen et al., 2021; Fang et al., 2022; Hu HT et al., 2022). Fig. 1a shows the radar plots for three different packaging antenna technologies. Packaging antenna typically uses printed circuit boards (PCBs); however, the dimension cannot be made small enough due to process constraints, and the performance of the antenna is affected by the large interconnections between the device and PCBs (Su et al., 2022). Importantly, the dimension of device package is often over-engineered to match the fabrication error (>40 μm) (Su et al., 2022). Recently, through-silicon via (TSV) has become a popular technology for packaging antennas. It has a precise microelectronic process and low manufacturing process error, which can meet the application needs of smaller interconnection length and shorter electrical delay (Watanabe et al., 2020; Xia et al., 2020; Yao et al., 2020). Nonetheless, silicon is a semiconductor material and produces intolerable signal loss at high frequencies. When the transmission line transmits through the signal, the signal and the substrate material produce a strong electromagnetic coupling effect, and the eddy current phenomenon occurs in the substrate, resulting in poor signal integrity (Watanabe et al., 2020; Xia et al., 2020; Yao et al., 2020; Chen et al., 2021). Through-glass vias (TGVs) have been widely investigated due to their ability to from fine-pitch line and their coefficient of thermal expansion (CTE) matching that of silicon (Watanabe et al., 2020; Xia et al., 2020). Besides, they present low signal loss tangent at high frequencies (0.0025 at 33 GHz), adjustable dielectric constant (Dk) that can vary from 3.78 to 8 ppm/K, and manufacturability of ultra-thin processing (CTE and Dk can be tailored depending on the materials used for integrated circuits (ICs) and PCBs) (Watanabe et al., 2020; Xia et al., 2020; Su et al., 2022). Meanwhile, TGVs can be prepared by laser-induced wet etching at low temperature to reduce the surface wave effect. The fabrication error of TGVs and redistribution layer (RDL) is low (<10 μm), and the thickness of glass substrate can be controlled between 50 μm and 2.5 mm to match the application requirements (Watanabe et al., 2020; Xia et al., 2020). Many researchers have carried out TGV-related research, such as glass-based integrated waveguide, filters, and radio frequency (RF) module (Watanabe et al., 2020; Xia et al., 2020). Fang et al. (2022) studied the properties of glass materials and made progress in reducing microwave loss tangent, which can well address the shortage in the low-loss glass material supply chain (Watanabe et al., 2020; Xia et al., 2020).

Recently, filtering antenna has been studied extensively because it can effectively reduce the system volume and loss (Zhang XY et al., 2015, 2017; Hu PF et al., 2016, 2019; Jin et al., 2018; Li JF et al., 2018, 2021; Wu et al., 2018; Zhang BH and Xue, 2018;

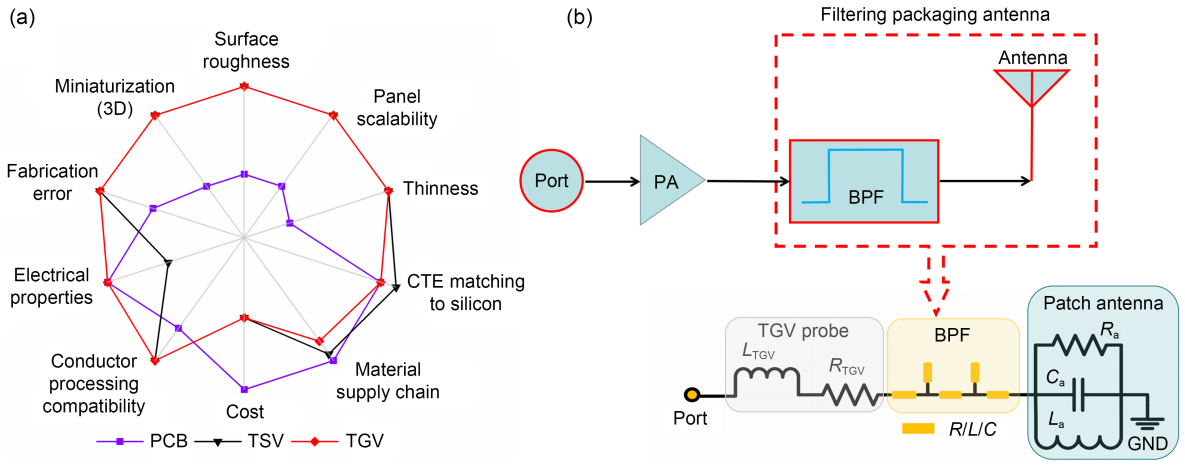

Fig. 1 Comparison and schematic of three primary substrate materials used for 5G millimeter-wave applications (a) and the proposed FPA connected to the power amplifier of a transmitter and the equivalent circuits (b) (FPA: filtering packaging antenna; PCB: printed circuit board; TSV: through-silicon via; TGV: through-glass via; CTE: coefficient of thermal expansion; PA: power amplifier; BPF: bandpass filter)

Hu KZ et al., 2020; Liu et al., 2020; Hu HT et al., 2022). The filtering antenna promotes the development of packaging antenna (Zhang XY et al., 2015, 2017; Hu PF et al., 2016, 2019; Jin et al., 2018; Li JF et al., 2018, 2021; Wu et al., 2018; Zhang BH and Xue, 2018; Hu KZ et al., 2020; Liu et al., 2020). As shown in Fig. 1b, the antenna and filter of a transmitter are usually connected to a power amplifier (PA). The design of filtering antenna includes the following aspects: first, the antenna feeder is used to obtain the filtering response (Hu PF et al., 2016; Zhang XY et al., 2017). It is necessary to cascade the filter circuit in the front section of feeder, which results in large size and complex structure. Second, the traditional filter synthesis method is adopted, and the antenna needs to be designed according to the coupling matrix theory (Wu et al., 2018; Zhang BH and Xue, 2018). Finally, some parasitic elements are introduced into the patch antenna to change the current distribution (Jin et al., 2018; Li JF et al., 2018; Hu PF et al., 2019; Liu et al., 2020). Thus, the antenna can obtain filtering response and effectively expand the bandwidth, which is highly suitable for preparing a miniaturized antenna. However, all of the filtering antennas mentioned above work only in S-band or C-band. The vast majority of the filtering antennas are made using PCBs, which limits the miniaturization ability and three-dimensional (3D) packaging of antennas. To the best knowledge of the authors, however, neither filtering antennas for Ka-band nor TGV-based filtering antennas have been published so far. This study is the first to integrate TGV technology into the design of filtering antennas. Of note, in a recent study, a filtering antenna was designed that works in V-band based on PCBs (Hu HT et al., 2022). An impedance bandwidth of 15% and radiation efficiency of 92% were obtained, and the out-of-band suppression also met the application requirements. However, this filtering antenna has a large volume ($>0.286\lambda_0^3$, where λ_0 is the guide wavelength), and its structure is overly complex.

This work presents the design and demonstration of a 33-GHz filtering antenna-in-package (AiP) module with broadband, which induces four radiating nulls to improve the suppression level in the stopband based on TGVs. The entire filtering packaging antenna (FPA) is stacked by three layers of glass substrate. The upper surface of layer 1 (radiation patch layer) is the radiation patch of the antenna, and the lower surface is the ground plane. Layer 2 is a glass transition layer introduced for signal interconnection between layer 1 and layer 3. Layer 3 is the signal feed layer, i.e., substrate integrated waveguide (SIW) transition feeding structure layer, of the entire FPA. Electrical interconnection of this three-layer structure is achieved using laser bonding interconnections. The signal is transmitted to the SIW transition feeding structure layer through a waveguide coaxial converter, and then fed to the antenna radiation patch through TGV interconnection, thereby realizing the conversion of the wireless signal. When considering the insertion loss and the reliability of the feed connection, TGV undoubtedly shows superiority in high-frequency performance (Hu HT et al., 2022). Compared with the coupling feed, TGV is more stable and is less affected by the environment. Impedance control of TGVs and pads is the key to achieving impedance matching and high bandwidth of the entire FPA. Specifically, the impedance of the antenna radiation patch should be designed to be slightly lower than 50 Ω with a capacitive impedance component (Ansoft HFSS ver. 11). This is because TGV usually introduces additional resistive and inductive components (Fig. 1b) (Li WL et al., 2023).

2 Materials and methods

The fabrication process of the FPA of this work is shown in Fig. 2. Our fabrication method enables high-density low-loss interconnections (Ka-band) and high-precision RDLs on glass substrate. Glass substrate with a thickness of ~650 μm and a surface roughness of less than 10 nm was prepared by a solid-phase reaction method. TGVs with a diameter of 60 μm were formed on the glass substrate by laser-induced etching (step 1). The glass substrate preparation process and the laser-induced etching were described in detail in Fang et al. (2022), which are repeated here. Through the single-side sputtering (step 2), electroplating (step 3), and polishing (step 4) processes, glass substrate with copper-filled TGVs was obtained, and the surface had no metal layer. Via double-side sputtering (step 5) and photolithography (step 6), metal patterns (including pads) on the surface of the glass substrate were formed (step 6). Then, the antenna radiation patch layer and the glass transition layer with

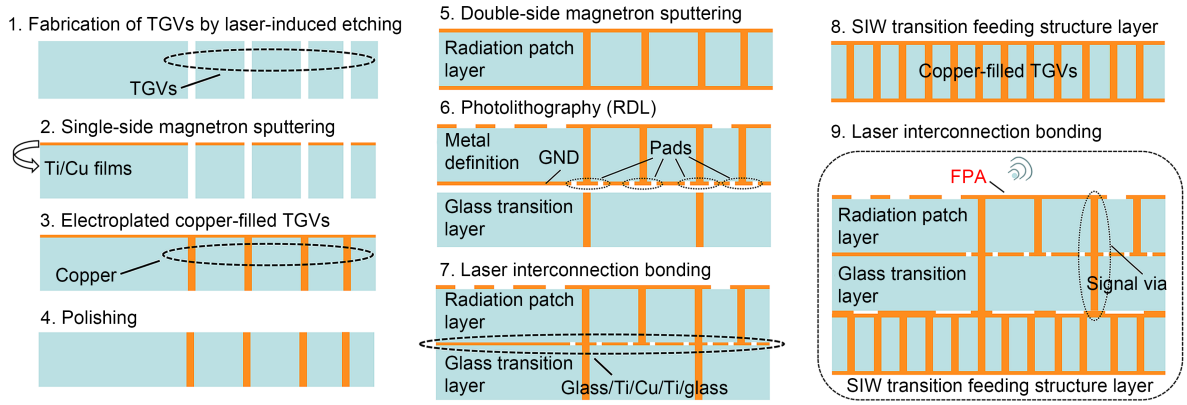

Fig. 2 Fabrication process of the proposed FPA (FPA: filtering packaging antenna; TGV: through-glass via; RDL: redistribution layer; SIW: substrate integrated waveguide)

copper-filled TGVs were bonded through laser interconnection (step 7) to achieve signal interconnection and physical support (the bonding interface was glass/Ti/Cu/Ti/glass). Finally, the laser interconnection bonding was realized between the SIW transition feeding structure layer (step 8) and the backside of layer 2 (step 9).

2.1 Magnetron sputtering (step 2)

First, a layer of an intermediate layer metal (titanium) of about 100-nm thickness was sputtered on the glass surface using magnetron sputtering equipment (JGP-450 of SKY Technology Development Co., Ltd., Chinese Academy of Sciences, China). The sputtering conditions were as follows: the sputtering atmosphere was 60 sccm of argon, the sputtering pressure was 1 Pa, the sputtering power was 250 W, and the sputtering time was 5 min. Immediately, after the sputtering of copper film layer (2 μm), the sputtering atmosphere was 60 sccm of argon, the sputtering pressure was 1 Pa, the sputtering power was 150 W, and the sputtering time was 120 min.

2.2 Electroplated copper-filled TGVs and polishing (steps 3 and 4)

The glass substrate after single-side sputtering of titanium or copper was transferred to an electroplating tank with electroplating solution with the current of 0.1 A/cm^2, and taken out after 72 h of electroplating. The formulation of the plating solution was as follows: the main contents were 67.4 g/L copper sulfate solution and 157 g/L sulfuric acid solution. The additives were inhibitor, leveler, and accelerator at 10, 12, and 0.8 ml/L, respectively. After being taken out, it was ground by a polishing machine for 2 h to obtain a bright glass substrate with copper-filled TGVs. Then, a copper-filled TGV glass substrate covered with titanium and copper films was obtained by magnetron sputtering.

2.3 Photolithography (step 6, RDL formation)

The patterning of the surface metal of the antenna radiation patch layer and the SIW transition feeding structure layer was obtained by photolithography. The pattern on the specific mask plate was copied to the photosensitive glass by the photolithography machine (URE-2000B, Institute of Optoelectronics Technology, Chinese Academy of Sciences, China). Meanwhile, alignment marks needed to be designed in advance. The parameters of the photolithography were as follows: first, we used a spin coater to evenly cover the surface of the copper film with the photoresist (AZ4620), which was then left to dry. After an exposure time duration of 15 s, it was transferred to the developer to remove the excess photoresist. Then, the glass substrate was soaked in nitric acid solution for 2 s and taken out immediately to remove excess copper films. Subsequently, it was transferred to a hydrogen peroxide solution at 90 °C for 10 s and taken out to remove the excess titanium films.

2.4 Laser interconnection bonding (step 7, metal–glass bonding)

The radiation patch layer was connected to the SIW transition feeding structure layer by a glass transition layer bonding process with many pads. In the

process of photolithography, we designed the size (radius of 50 μm) and position of the pad on the mask in advance. Only metal patterns and pads were left on the glass substrate through photolithography. The SIW transition feeding structure layer and the glass transition layer were aligned and pressed (the applied pressure was 1 MPa) using a bonding interconnection alignment machine, fixed by a specific model, and finally placed on a laser bonding machine to achieve bonding between metal and glass (the energy of the laser was 3 W). Similarly, the bonded SIW transition feeding structure layer and glass transition layer were bonded to the antenna radiation patch layer.

3 Results

3.1 Radiation patch layer design

Fig. 3 illustrates the configuration of the proposed antenna radiation patch layer, which consists of two $\lambda_g/2$ defect ground structures (DGSs) and three pairs of $\lambda_g/4$ defect microstrip structures (DMSs). The glass substrate has a relative permittivity of 4.8 and dielectric loss tangent of 0.0025 at 33 GHz. The thickness of the glass substrate is 0.56 mm. Meanwhile, the input impedance of the antenna can be changed by varying the position of the TGV feed to match the impedance of the 50-Ω RF circuit. A pair of slots are etched on the ground plane to change the electric field distribution on the ground. In addition, a circle is etched around the TGV signal to prevent the signal from being transmitted to the ground.

The distance from the TGV to the center can be approximated according to the characteristic impedance calculation of the coaxial line in Eq. (1):

$$R = \exp\left(\frac{Z_0\sqrt{\varepsilon_r}}{60}\right)r, \tag{1}$$

where R represents the distance from the outer conductor to the center, Z_0 represents the characteristic impedance, $\sqrt{\varepsilon_r}$ is the dielectric constant of the glass substrate, and r represents the radius of the inner conductor. According to the process, when r is 30 μm, the R calculated is about 150 μm. The radiation nulls are designed according to the frequency f_{null}. Three pairs of slots are etched on the radiation patch, resulting in three radiation nulls on both sides of the passband (DMS). The radiation nulls (null 1, null 3, and null 4) are produced by comparing the length of the corresponding slots L. These slots operate at quarter wavelength resonance, so the radiation null frequency can be evaluated as

$$f_{null} \approx \frac{c}{4L\sqrt{\varepsilon_r}}, \tag{2}$$

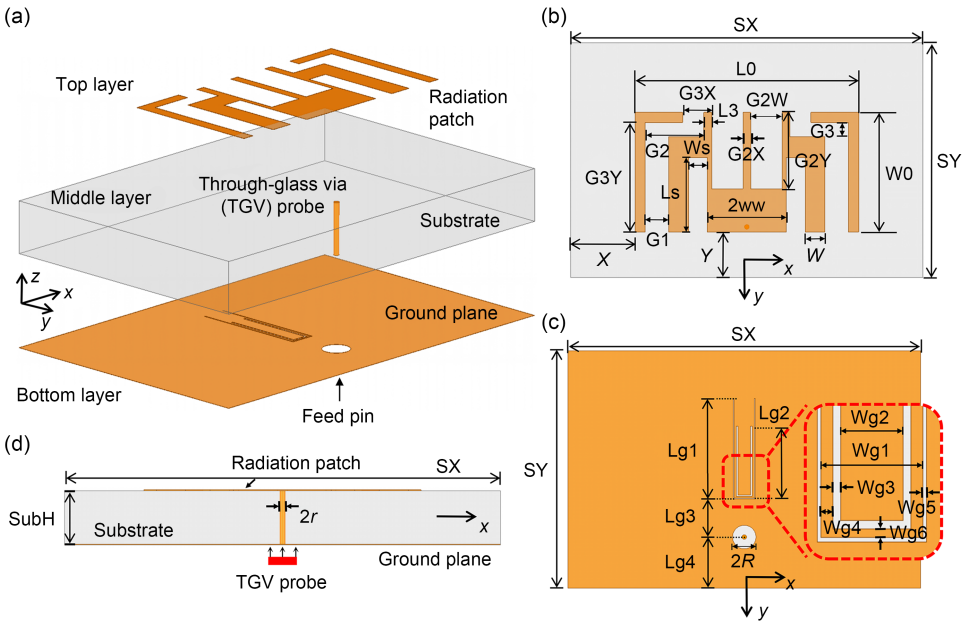

Fig. 3 Geometry of the proposed filtering packaging antenna: (a) exploded view; (b) top view; (c) bottom view; (d) side view

where c represents the speed of light. Null 2 is caused by etching two U-shaped slots in the ground plane (DGS). The region between the central resonator and the slotted patches is above the two U-shaped slots. The final optimized size is shown in Table 1.

Table 1 Parameters of the filtering packaging antenna

Para.	Value (mm)	Para.	Value (mm)	Para.	Value (mm)
T	0.002	SX	4.500	SY	3
L0	2.862	W0	1.529	SubH	0.560
Ls	0.950	Ws	0.240	ww	0.506
G2X	0.100	G2Y	0.977	G2W	0.400
G3Y	1.400	G3X	0.370	G1	0.300
G2	0.750	G3	0.182	L3	0.100
Lg1	1.270	Lg2	0.890	Lg3	0.483
Lg4	0.647	Wg1	0.260	Wg2	0.160
Wg3	0.020	Wg4	0.030	Wg5	0.010
Wg6	0.020	R	0.150	r	0.030
X	0.819	Y	0.582	W	0.254

3.2 SIW transition feeding structure

In an actual microwave circuit system, the proposed filtering antenna is controlled by RF chips embedded in the middle layer (transmitting signals through TGVs). However, an SIW transition feeding structure is used for the convenience of measuring the far-field radiation performance, as shown in Fig. 4a. The signal is transmitted to the SIW using a waveguide coaxial converter (26.5–40 GHz, HD-320WCAK). The radiation patch layer provides electrical interconnection to the SIW transition feeding structure layer by a glass transition layer formed by laser bonding process using a pad and a TGV. Fig. 4c illustrates the configuration of the proposed SIW transition feeding structure layer, where the SIW has been deliberately designed to work in an ultra-wide frequency band, making sure that the cutoff frequency is lower than the passband frequency of the proposed antenna. The −10-dB impedance bandwidth ranges from 25 to over 45 GHz, while the insertion loss in the antenna passband is below 0.6 dB. The final optimized size of the SIW transition feeding structure is shown in Table 2.

3.3 Operation principle

3.3.1 Resonant point

To intuitively illustrate the amplitude module, Fig. 5a depicts the simulated E-field distributions on the SIW transition feeding structure. Since the SIW structure can transmit only TE_{n0} (n>0) mode and

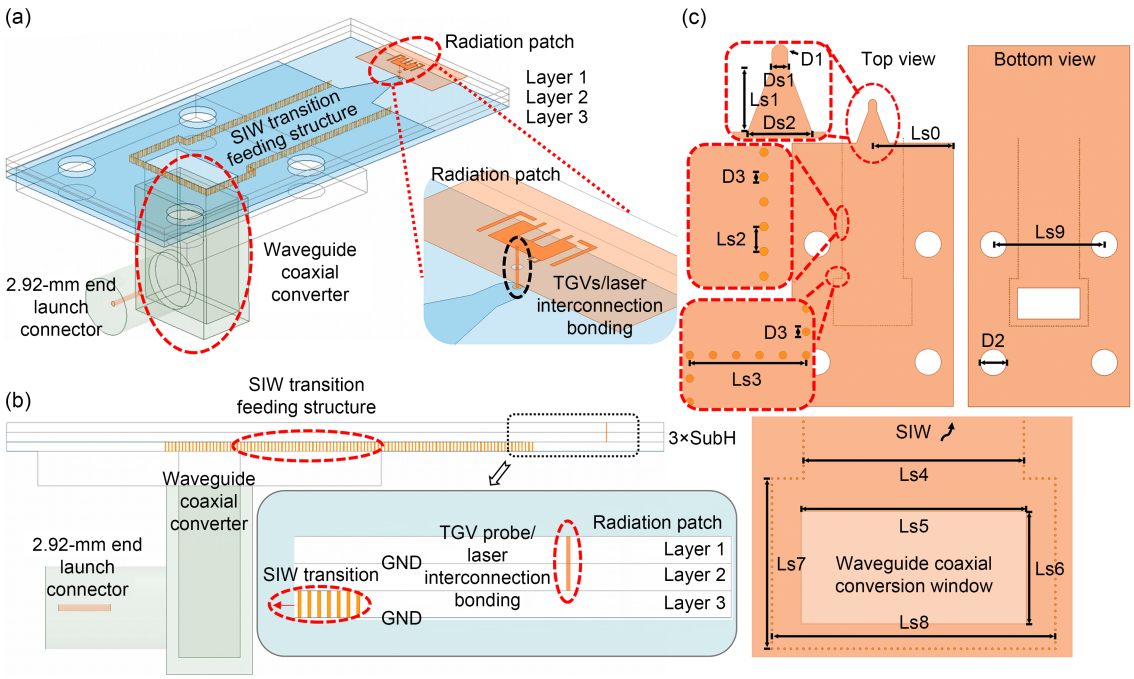

Fig. 4 Geometry of the proposed filtering packaging antenna (FPA) with substrate integrated waveguide (SIW) transition feeding structure: (a) exploded view; (b) side view; (c) SIW transition feeding structure

Table 2 Parameters of the substrate integrated waveguide transition feeding structure

Parameter	Value (mm)	Parameter	Value (mm)
Thickness	0.002	D1	0.928
D2	3.000	D3	0.070
Ds1	0.928	Ds2	3.700
Ls0	9.250	Ls1	3.700
Ls2	0.200	Ls3	1.000
Ls4	7.000	Ls5	7.150
Ls6	3.580	Ls7	5.400
Ls8	9.000	Ls9	12.700

the radiation patch is fed by SIW, we can reveal the mechanism of antenna resonant points as long as we analyze the transmission mode in SIW. As shown in Fig. 5b, only the TE_{10} mode flows into the antenna through the SIW transition, and a higher mode cannot be transmitted. Hence, the resonant points in the antenna passband are generated by the TE_{10} mode. Furthermore, as shown in Fig. 5c, the current distributions of the TE_{10} mode are symmetrical along the *x* axis at 31.2 and 35 GHz. This is because only the TE_{10} mode flows into the antenna through the SIW transition, and the currents of the TE_{10} mode distributed along the *x* axis of the radiation patch are cut off by the slots.

3.3.2 Four radiation nulls

To gain some insights into the radiation nulls of the proposed FPA, the simulated current distributions at null 1 (25.6 GHz), null 2 (27.2 GHz), null 3 (38 GHz), null 4 (42.1 GHz), and the central frequency (33 GHz) are compared in Figs. 6–8. For symmetry and visibility, only the partial current distribution of the radiation patch is given. With reference to Fig. 6, the strong flows of patch currents in opposite currents are observed at the edges of the patch. The destructive superposition of the radiation field from the opposite current gives rise to null 1. However, there is a strong flow of patch currents in the same direction at the central frequency (33 GHz), in which the radiated fields are constructively superimposed. Similarly, because the radiation patch radiates upward, it is partly generated by ground reflection, as shown in Fig. 7. At 27.2 GHz, the electromagnetic wave radiated by the main body is in the opposite phase to the electromagnetic wave reflected from the ground, which also produces a destructive superimposed radiation field that is responsible for null 2. As shown in Fig. 8, null 3 and null 4 are also caused by the same principle.

3.4 *S*-parameter analysis of TGVs

In this part, *S*-parameters of TGV (diameter of 65 μm, height of 1.68 mm) and PCB (Rogers 5880) via (diameter of 65 μm, height of 1.68 mm) are extracted and compared. As shown in Fig. 9, the simulation model seeks to realize the interconnection of three layers of substrate by microstrip line and vias. In addition, the diameter of the grounding shield column is 200 μm to ensure the smooth impedance transition of the signal transmission via and reduce signal distortion (Li WL et al., 2023). Li WL et al. (2023) proposed seven shielding patterns to realize the high isolation capability and diversified application of glass interposer, and discussed the influence of the grounding shield column around the signal via on the transmission characteristics. Compared with the single microstrip line, the *S*-parameter of the vias was extracted. Figs. 9a and 9b present the PCB via simulation model and the TGV simulation model, respectively.

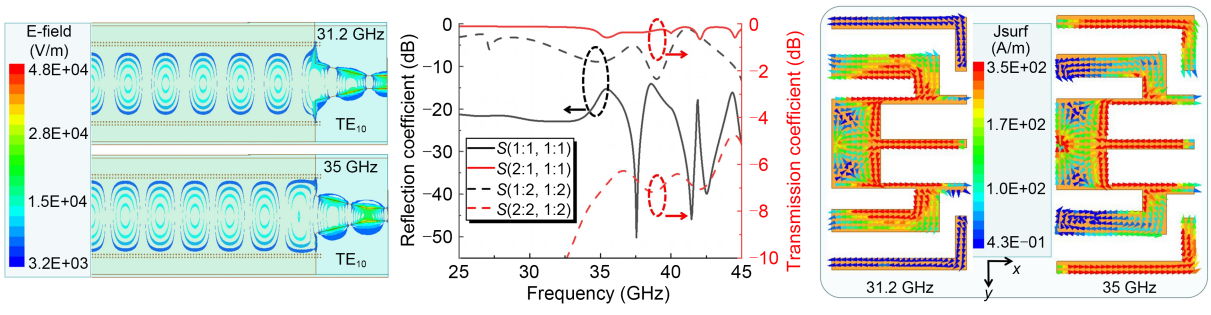

(a) (b) (c)

Fig. 5 Operation principle of the resonant point in the passband: (a) E-field distributions on the substrate integrated waveguide (SIW); (b) simulated performance of the SIW transition feeding structure; (c) simulated current distributions on the radiation patch at the resonant point

The comparison in Fig. 9c reveals that there is little difference in the low frequency band (<10 GHz), and that the advantages of TGV are not obvious. However, in the high frequency band (10–40 GHz), the insertion loss of TGV is much smaller, and the maximum is 0.3 dB at 33 GHz. The lower insertion loss in the high frequency band can effectively increase the radiation efficiency of the antenna. This establishes TGV as one of the best options for antenna radiation materials in the high frequency band.

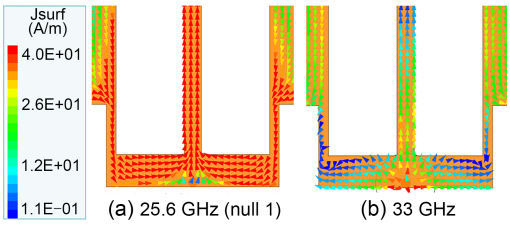

Fig. 6 Simulated current distributions on the radiation patches at radiation null frequency $f_{\text{null 1}}$ 25.6 GHz (a) and central frequency 33 GHz (b)

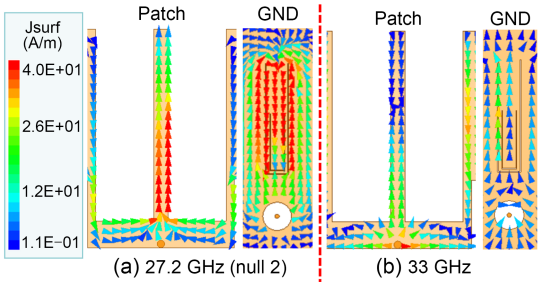

Fig. 7 Simulated current distributions on the radiation patches at radiation null frequency $f_{\text{null 2}}$ 27.2 GHz (a) and central frequency 33 GHz (b)

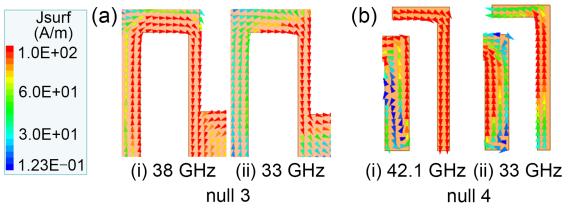

Fig. 8 Simulated current distributions on the radiation patches at radiation null frequency $f_{\text{null 3}}$ 38 GHz (a) and radiation null frequency $f_{\text{null 4}}$ 42.1 GHz (b)

3.5 Measurement and simulation results

In this work, the reflection coefficient $|S_{11}|$ was measured by an Agilent Technologies N5234A PNA-L network analyzer (10 MHz–43.5 GHz). The radiation performance was quantified in an indoor far-field measurement chamber. The far-field radiation performance of the proposed antenna can be determined according to the excitation power provided by the signal source and the power measured by the spectrum analyzer, combined with the gain of the standard gain horn (SGH).

Fig. 10 illustrates that the proposed antenna was fabricated using TGV and micro-electro-mechanical system (MEMS) technology. Two substrates (50.8 mm×50.8 mm×0.56 mm) with copper-filled TGVs and surface metal patterns were first fabricated separately, and then the SIW transition layer (5-μm thick copper) and the radiation patch were connected through an intermediate glass transition layer (50.8 mm×50.8 mm×0.56 mm) using a laser bonding technique under appropriate temperature and pressure conditions. The specific process is shown in Fig. 2. The final prototype was coated with copper resistant oxidant to achieve high reliability. Fig. 10g illustrates the proposed FPA fabricated prototypes (50.8 mm×50.8 mm×1.689 mm), which were measured in an indoor far-field chamber.

Fig. 11 illustrates that compared to the Ref_antenna (a traditional rectangular patch), the proposed FPA has

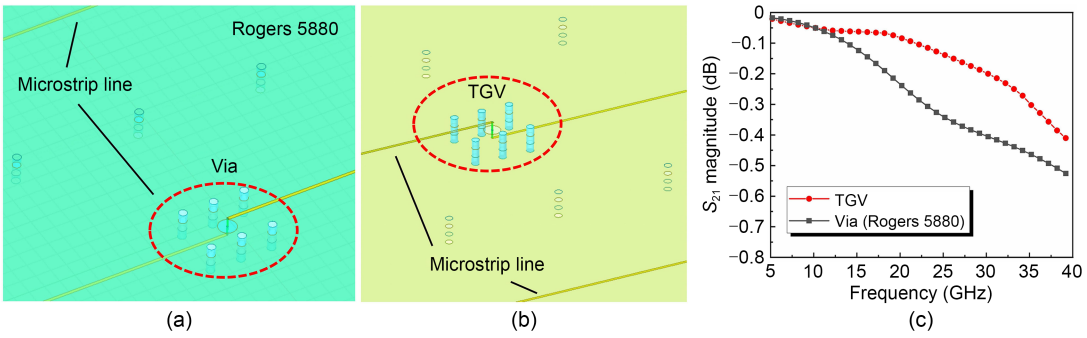

Fig. 9 *S*-parameter analysis: (a) printed circuit board (PCB, Rogers 5880) via simulation model; (b) through-glass via (TGV) simulation model; (c) *S*-parameters of the TGV and via

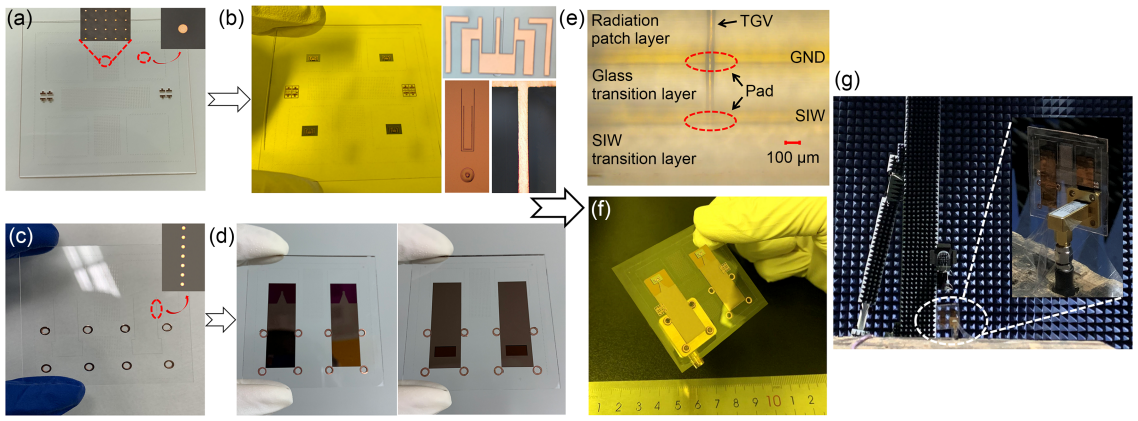

Fig. 10 Fabricated prototypes of the proposed filtering packaging antenna (FPA): (a) diagram of the radiation patch layer of copper-filled through-glass vias (TGVs); (b) the fabricated prototypes of the radiation patch layer (top view, bottom view, and side view of TGVs); (c) diagram of the substrate integrated waveguide (SIW) transition feeding layer of copper-filled TGVs; (d) the fabricated prototypes of SIW transition feeding layer; (e) side view of interconnection bonding; (f) final prototype; (g) radiation performance measured in an indoor far-field chamber

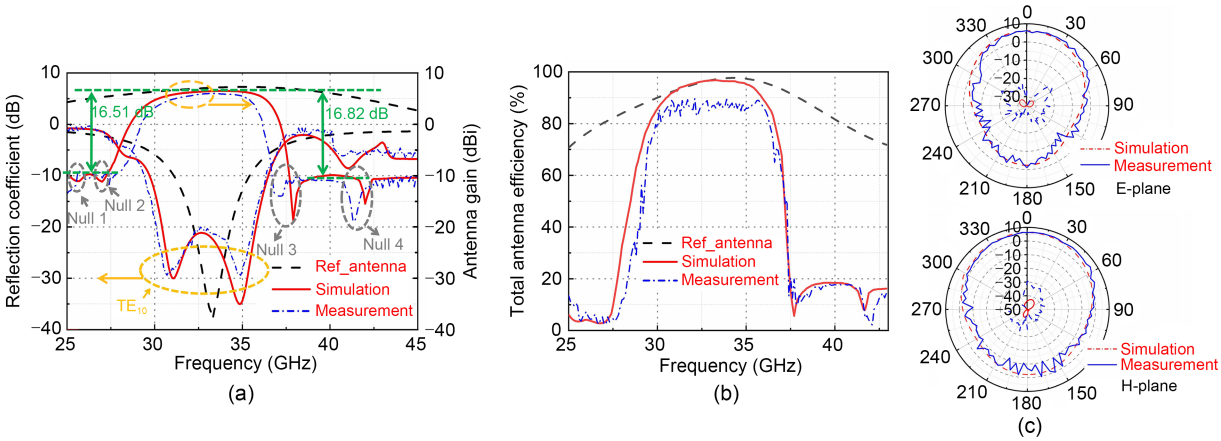

Fig. 11 Measurement and simulation results of reflection coefficient and antenna gain (θ=0°) (a), radiation efficiency (b), and radiation patterns at 33 GHz (c)

enhanced bandwidth and filtering characteristics. Furthermore, it has four radiation nulls for the band-edge, which improves the suppression level in the stopband. The measurement results show that the impedance is matched from 29.4 to 36.4 GHz, with the measurement out-of-band suppression being higher than 16.51 and 16.82 dB for the lower and upper stopbands, respectively (Fig. 11a). The measurement peak realized gain is ~6.5 dBi. Fig. 11b illustrates the measurement and simulation results of radiation efficiency for the proposed antenna. The measurement radiation efficiency is less than 90%, which may cause ohmic loss in the FPA prototype. Fig. 11c illustrates the measurement and simulation radiation patterns at the central frequency (33 GHz). The maximum co-polar field is found in the boresight direction (θ=0°). The measurement radiation patterns of E-plane and H-plane have a large deviation from the simulation results, which is caused by experimental imperfections including assembly errors. According to the measurement data, the application requirements of the system are met.

4 Discussion

The proposed filtering antenna has been quantitatively compared with some fabricated packaging antennas (Table 3) and filtering antennas (Table 4). As shown in Table 3, compared with PCB-packaged antennas, glass-packaged antennas exhibit obvious advantages

Table 3 Comparison with packaging antennas

Reference	Fabrication technology	Integration level	Antenna dimension	Bandwidth	Feed type	Antenna type	Gain (dBi)
Hwang et al., 2017	PCB	Middle	$0.009\lambda_0^3$	9.3%	Coplanar stripline	Yagi-Uda	5.7
El-Halwagy et al., 2018	PCB	Middle	$0.09\lambda_0^3$	25.7%	SIW	SIW dipole	4.5
Yao et al., 2020	Si (WLP)	High	$4.1\lambda_0^3$	28%	Waveguide	Horn	
Watanabe et al., 2020	Glass	High	$0.004\lambda_0^3$	28.2%	TGVs	Yagi-Uda	4.8
Xia et al., 2020	Glass	High	$0.049\lambda_0^3$	33%	CPW-slotline	Taper-slot	3.5
This work	Glass	High	$0.1\lambda_0^3$	21.2%	SIW+TGVs	Filtenna	6.5

λ_0: guide wavelength; PCB: printed circuit board; SIW: substrate integrated waveguide; TGV: through-glass via; CPW: coplanar waveguide

Table 4 Comparison with filtering antennas

Reference	Antenna dimension	Number	Bandwidth	Feed type	Gain (dBi)	Suppression level (dB)	Efficiency (%)
Hu HT et al., 2022	$>0.2864\lambda_0^3$	2	15%	Coupling	7.9	19.1	92
Li JF et al., 2018	$0.021\lambda_0^3$	2	23.5%	Coaxial	6.8	>17	
Jin et al., 2018	$0.012\lambda_0^3$	1	7%	Coaxial	6.6	>11	80
Hu PF et al., 2019	$0.029\lambda_0^3$	2	23.1%	F-shaped probe	8.2	>21	72.7
Liu et al., 2020	$0.0169\lambda_0^3$	1	5.86%	Coaxial	6.28	>17	72.5
Li JF et al., 2021	$0.022\lambda_0^3$	2	19.4%	Coaxial	6	>15	75
Hu KZ et al., 2020	$0.005\lambda_0^3$	1	5.1%	Microstrip	6.3	13	
This work	$0.1\lambda_0^3$	3	21.2%	SIW+TGVs	6.5	>16.5	89.5

λ_0: guide wavelength; number: the number of substrate layers; SIW: substrate integrated waveguide; TGV: through-glass via

in the millimeter-wave frequency band. These include mainly low-loss transmission, high-density integration, and a more precise manufacturing process. In addition, although silicon package (TSV) has a higher integration level than TGV, the intolerable transmission loss at high frequency has become the main factor limiting its development. As an enhancement to the glass-packaged antenna type, this work introduces a three-layer glass stack structure to achieve signal interconnection by laser metal–glass bonding technology. The 3D integrated packaging of the antenna is realized, which effectively reduces the insertion loss of the signal during the transmission process and lowers the process cost, as shown in Table 4. Since the proposed antenna adopts SIW combined with TGV feed, it undoubtedly shows superiority in high-frequency performance when considering the insertion loss and reliability of feed connection. The filtering antenna is also the AiP type because the manufacturing process entails the fusion of TGV technology and MEMS technology. The antenna structure requires only three glass substrates, which reduces the complexity and cost of fabrication. In addition, the proposed antenna introduces four radiation nulls in the stopband, and obtains a sufficient level of out-of-band signal suppression. As a whole, the FPA is particularly suitable for millimeter-wave communication systems.

5 Conclusions

The innovation of this work in the research of glass 3D packaging antennas is a novel laser interconnection bonding scheme to realize a low-cost, high-density 3D interconnected structure. By combining the glass packaging antenna and the filtering antenna design, this work achieves high-performance 3D stack miniaturization and filter response in the Ka-band. In addition, the introduction of four radiation nulls can effectively improve the suppression level in the stopband. Overall, this work presents an FPA with three layers of glass bonding interconnection and assembly, which is particularly suitable for millimeter-wave receiving or transmitting circuit systems.

Contributors

Zhen FANG and Jihua ZHANG designed the research. Zhen FANG, Hongwei CHEN, and Libin GAO processed the data. Zhen FANG drafted the paper. Wenlei LI and Tianpeng LIANG helped organize the paper. Zhen FANG, Xudong CAI, Xingzhou CAI, Weicong JIA, Huan GUO, and Yong LI helped

complete the antenna prototype preparation, assembly, and testing. Jihua ZHANG and Zhen FANG revised and finalized the paper.

Compliance with ethics guidelines

Zhen FANG, Jihua ZHANG, Libin GAO, Hongwei CHEN, Wenlei LI, Tianpeng LIANG, Xudong CAI, Xingzhou CAI, Weicong JIA, Huan GUO, and Yong LI declare that they have no conflict of interest.

Data availability

The data that support the findings of this study are available from the corresponding author upon reasonable request.

References

Cao YF, Zhang Y, Zhang XY, 2020. Filtering antennas: from innovative concepts to industrial applications. *Front Inform Technol Electron Eng*, 21(1):116-127. https://doi.org/10.1631/FITEE.1900474

Chen L, Yang XF, Yu DQ, 2021. Development of through glass via technology. *Electr Packag*, 21(4):040101 (in Chinese).

El-Halwagy W, Mirzavand R, Melzer J, et al., 2018. Investigation of wideband substrate-integrated vertically-polarized electric dipole antenna and arrays for mm-wave 5G mobile devices. *IEEE Access*, 6:2145-2157. https://doi.org/10.1109/ACCESS.2017.2782083

Fang Z, Gao LB, Chen HW, et al., 2022. 3D interdigital electrodes dielectric capacitor array for energy storage based on through glass vias. *Adv Mater Technol*, 7(8):2101530. https://doi.org/10.1002/admt.202101530

He YQ, Rao ML, Liu YJ, et al., 2020. 28/39-GHz dual-band dual-polarized millimeter wave stacked patch antenna array for 5G applications. Int Workshop on Antenna Technology, p.1-4. https://doi.org/10.1109/iWAT48004.2020.1570609770

Hu HT, Chan KF, Chan CH, 2022. 60 GHz Fabry–Pérot cavity filtering antenna driven by an SIW-fed filtering source. *IEEE Trans Antenn Propag*, 70(2):823-834. https://doi.org/10.1109/TAP.2021.3111277

Hu KZ, Tang MC, Li DJ, et al., 2020. Design of compact, single-layered substrate integrated waveguide filtenna with parasitic patch. *IEEE Trans Antenn Propag*, 68(2):1134-1139. https://doi.org/10.1109/TAP.2019.2938574

Hu PF, Pan YM, Zhang XY, et al., 2016. A compact filtering dielectric resonator antenna with wide bandwidth and high gain. *IEEE Trans Antenn Propag*, 64(8):3645-3651. https://doi.org/10.1109/TAP.2016.2565733

Hu PF, Pan YM, Zhang XY, et al., 2019. A filtering patch antenna with reconfigurable frequency and bandwidth using F-shaped probe. *IEEE Trans Antenn Propag*, 67(1):121-130. https://doi.org/10.1109/TAP.2018.2877301

Hwang IJ, Jo HW, Kim JW, et al., 2017. Vertically stacked folded dipole antenna using multi-layer for mm-wave mobile terminals. IEEE Int Symp on Antennas and Propagation & USNC/URSI National Radio Science Meeting, p.2579-2580. https://doi.org/10.1109/apusncursinrsm.2017.8073332

Jin JY, Liao SW, Xue Q, 2018. Design of filtering-radiating patch antennas with tunable radiation nulls for high selectivity. *IEEE Trans Antenn Propag*, 66(4):2125-2130. https://doi.org/10.1109/TAP.2018.2804661

Li JF, Chen ZN, Wu DL, et al., 2018. Dual-beam filtering patch antennas for wireless communication application. *IEEE Trans Antenn Propag*, 66(7):3730-3734. https://doi.org/10.1109/TAP.2018.2835519

Li JF, Mao CX, Wu DL, et al., 2021. A dual-beam wideband filtering patch antenna with absorptive band-edge radiation nulls. *IEEE Trans Antenn Propag*, 69(12):8926-8931. https://doi.org/10.1109/TAP.2021.3097359

Li WL, Zhang JH, Gao LB, et al., 2023. Wideband analysis and prolongation of surrounding TGVs shielding structure in 3-D ICs. *IEEE Microw Wirel Technol Lett*, 33(1):39-42. https://doi.org/10.1109/LMWC.2022.3201523

Li WX, Xu KD, Tang XH, et al., 2017. Substrate integrated waveguide cavity-backed slot array antenna using high-order radiation modes for dual-band applications in K-band. *IEEE Trans Antenn Propag*, 65(9):4556-4565. https://doi.org/10.1109/TAP.2017.2723089

Liu YT, Leung KW, Yang N, 2020. Compact absorptive filtering patch antenna. *IEEE Trans Antenn Propag*, 68(2):633-642. https://doi.org/10.1109/TAP.2019.2938798

Shah U, Liljeholm J, Campion J, et al., 2018. Low-loss, high-linearity RF interposers enabled by through glass vias. *IEEE Microw Wirel Compon Lett*, 28(11):960-962. https://doi.org/10.1109/LMWC.2018.2869285

Shao ZJ, Zhang YP, 2021. A single-layer miniaturized patch antenna based on coupled microstrips. *IEEE Antenn Wirel Propag Lett*, 20(5):823-827. https://doi.org/10.1109/LAWP.2021.3064908

Su YQ, Yu DQ, Ruan WB, et al., 2022. Development of compact millimeter-wave antenna by stacking of five glass wafers with through glass vias. *IEEE Electron Device Lett*, 43(6):934-937. https://doi.org/10.1109/LED.2022.3168877

Watanabe AO, Lin TH, Ali M, et al., 2020. Ultrathin antenna-integrated glass-based millimeter-wave package with through-glass vias. *IEEE Trans Microw Theory Techn*, 68(12):5082-5092. https://doi.org/10.1109/TMTT.2020.3022357

Wu QS, Zhang X, Zhu L, 2018. Co-design of a wideband circularly polarized filtering patch antenna with three minima in axial ratio response. *IEEE Trans Antenn Propag*, 66(10):5022-5030. https://doi.org/10.1109/TAP.2018.2856104

Xia HY, Zhang T, Li LM, et al., 2020. A 1×2 taper slot antenna array with flip-chip interconnect via glass-IPD technology for 60 GHz radar sensors. *IEEE Access*, 8:61790-61796. https://doi.org/10.1109/ACCESS.2020.2983485

Yao SS, Cheng YJ, Zhou MM, et al., 2020. D-band wideband air-filled plate array antenna with multistage impedance matching based on MEMS micromachining technology. *IEEE Trans Antenn Propag*, 68(6):4502-4511. https://doi.org/10.1109/TAP.2020.2969890

Zhang BH, Xue Q, 2018. Filtering antenna with high selectivity using multiple coupling paths from source/load to resonators. *IEEE Trans Antenn Propag*, 66(8):4320-4325. https://doi.org/10.1109/TAP.2018.2839968

Zhang XY, Duan W, Pan YM, 2015. High-gain filtering patch antenna without extra circuit. *IEEE Trans Antenn Propag*, 63(12):5883-5888. https://doi.org/10.1109/TAP.2015.2481484

Zhang XY, Zhang Y, Pan YM, et al., 2017. Low-profile dual-band filtering patch antenna and its application to LTE MIMO system. *IEEE Trans Antenn Propag*, 65(1):103-113. https://doi.org/10.1109/TAP.2016.2631218